

AD-A260 043



# Center for Night Vision and Electro-Optics

CONTRACT NUMBER

DAAK70-83-K-0047

REPORT NUMBER

NV-90-15

Title: Electroreflectance And Auto-  
matic Scanning Ellipsometry of  
Mercury Cadmium Telluride

Author: Dr. P. M. Raccah

Address: Univ. of Illinois at Chicago  
Dept. of Physics  
Box 4348  
Chicago, Illinois 60680

Type of Report: FINAL

Date: August 30, 1990  
Revised July 7, 1992

JAN 15 1993

93-00438



**DISTRIBUTION STATEMENT**

Approved for public release;  
Distribution Unlimited

FORT BELVOIR, VA 22060-5677

93 1 06 082

REPORT DOCUMENTATION PAGE				Form Approved OMB No. 0704-0188	
1a. REPORT SECURITY CLASSIFICATION <b>UNCLASSIFIED</b>			1b. RESTRICTIVE MARKINGS <b>UNLIMITED</b>		
2a. SECURITY CLASSIFICATION AUTHORITY			3. DISTRIBUTION / AVAILABILITY OF REPORT		
2b. DECLASSIFICATION / DOWNGRADING SCHEDULE					
4. PERFORMING ORGANIZATION REPORT NUMBER(S)			5. MONITORING ORGANIZATION REPORT NUMBER(S) <b>NV-90-15</b>		
6a. NAME OF PERFORMING ORGANIZATION <b>Univ. of Illinois at Chicago, Dept of Physics</b>		6b. OFFICE SYMBOL (if applicable)	7a. NAME OF MONITORING ORGANIZATION <b>U.S.A CECOM Center for Night Vision &amp; Electro-Optics,</b>		
6c. ADDRESS (City, State, and ZIP Code) <b>Box 4348 Chicago, Illinois 60680</b>			7b. ADDRESS (City, State, and ZIP Code) <b>ATTN: AMSEL-RD-NV-IT-EMRT Fort Belvoir, VA 22060-5677</b>		
8a. NAME OF FUNDING / SPONSORING ORGANIZATION		8b. OFFICE SYMBOL (if applicable)	9. PROCUREMENT INSTRUMENT IDENTIFICATION NUMBER <b>Contract #DAAK70-83-K-0047</b>		
8c. ADDRESS (City, State, and ZIP Code)			10. SOURCE OF FUNDING NUMBERS		
			PROGRAM ELEMENT NO. <b>61102A</b>	PROJECT NO <b>02A31B</b>	TASK NO. <b>HO</b>
11. TITLE (Include Security Classification) (U) <b>ELECTROLYTE ELECTROREFLECTANCE AND AUTOMATIC SCANNING ELLIPSOMETRY CHARACTERIZATION OF MERCURY CADMIUM TELLURIDE.</b>					
12. PERSONAL AUTHOR(S) <b>RACCAH, PAUL M.</b>					
13a. TYPE OF REPORT <b>FINAL</b>		13b. TIME COVERED FROM <b>82/2/1</b> TO <b>86/1/31</b>		14. DATE OF REPORT (Year, Month, Day) <b>July 9, 1990</b>	
15. PAGE COUNT <b>46</b>					
16. SUPPLEMENTARY NOTATION					
17. COSATI CODES			18. SUBJECT TERMS (Continue on reverse if necessary and identify by block number) <b>Optical characterization, electrolyte electro-reflectance (EER), automatic scanning ellipsometry (ASE), infrared detector materials (mercury cadmium</b>		
FIELD	GROUP	SUB-GROUP			
<b>9</b>	<b>1</b>	<b>8/2 &amp; 30</b>			
<b>20</b>	<b>12</b>	<b>5</b>			
19. ABSTRACT (Continue on reverse if necessary and identify by block number) <b>The optical characterization of bulk, epitaxial, and surface treated, e.g. oxidized, mercury cadmium telluride by electrolyte electroreflectance, automatic scanning ellipsometry, and reflectance were experimentally and theoretically unified to establish a basis for in situ nondestructive evaluation of composition, crystal quality, and surface and interface properties. Specifically, a generalized theory was developed and applied to yield a unified interpretation of experimental E1 transition energies and line widths and anomalies for the consistent determination of composition fraction, x-value, relative crystal quality, interface roughness, long range strain, and polarizability.</b>					
20. DISTRIBUTION / AVAILABILITY OF ABSTRACT <input checked="" type="checkbox"/> UNCLASSIFIED/UNLIMITED <input type="checkbox"/> SAME AS RPT. <input type="checkbox"/> DTIC USERS			21. ABSTRACT SECURITY CLASSIFICATION <b>UNCLASSIFIED</b>		
22a. NAME OF RESPONSIBLE INDIVIDUAL <b>Dr. Michael Martinka</b>			22b. TELEPHONE (Include Area Code) <b>703-664-5780</b>		22c. OFFICE SYMBOL <b>AMSEL-RD-NV-IT-EMRT</b>

NAME OF CONTRACTOR:	PAUL M. RACCAH
CONTRACT NUMBER:	DAAK 70-83-K-0047
SHORT TITLE:	EER & ASE CHARACTERIZATION OF MCT
EFFECTIVE DATE OF CONTRACT:	2/1/83
EXPIRATION DATE OF CONTRACT:	1/31/86
REPORTING PERIOD:	FINAL REPORT
PRINCIPAL INVESTIGATOR:	PAUL M. RACCAH
PHONE NUMBER:	(312) 996-3403

THE VIEWS AND CONCLUSIONS IN THIS DOCUMENT ARE THOSE OF THE AUTHORS AND SHOULD NOT BE INTERPRETED AS NECESSARILY REPRESENTING THE OFFICIAL POLICIES, EITHER EXPRESS OR IMPLIED, OF THE U.S. GOVERNMENT.

Accession For	
NTIS CRA&I	<input checked="" type="checkbox"/>
DTIC TAB	<input type="checkbox"/>
Unannounced	<input type="checkbox"/>
Justification .....	
By .....	
Distribution /	
Availability Codes	
Dist	Avail and/or Special
A-1	

DTIC QUALITY INSPECTED 1

## SUMMARY

The characterization studies of bulk and epitaxial Mercury Cadmium Telluride by electrolyte electroreflectance (EER) and automatic scanning ellipsometry (ASE) that have been undertaken in this investigation covered a number of distinct phases. Initially EER techniques that had proven highly successful for us in previous sample composition studies were extended to study anodic and plasma-deposited oxide layers on MCT samples. Coupled with SIMS data on these same samples a number of results were achieved. Parameters relating to composition, crystal quality, and carrier concentration as a function of depth were measured for oxides deposited on substrates grown by various techniques. These measurements allowed the quality of the semiconductor materials to be compared for various growth procedures and deposition techniques. Crystal damage was found not to be enhanced by oxide deposition but plasma deposition was found to have an effect on Hg depletion within the oxidized region.

The second phase of investigation was intended to extend the characterization studies to ASE. In this phase it was shown that ASE could be used to measure the surface roughness at the interface between the oxide and the semiconductor, the fraction of the oxide relative to the semiconductor in the rough layer, and the thickness of the oxide. The feasibility of studying the effects of chemical attacks on the surface was thus established.

The first two phases provided the impetus for the crucial third phase of study which involved unifying the EER and ASE measurements. A study of 7 NVL samples by both techniques revealed like measurements on  $E_1$  energies with best agreement recorded for LPE samples. Linewidth data, however, which is related to crystal quality differs for the two techniques. Comparative lineshape measurements from EER and ASE allowed the development of a generalized theory of EER (J. Vac. Sci. Technol. A, 3, 138 (1985)) and a newly proposed expression for the EER lineshape. Since electrorestriction and defect polarization are included in the generalized theory, the anomalous lineshapes observed provided a measure of long range strain and defect polarizability. This generalized theory exhibited its potential when EER was used to study the A and B faces of CdTe and revealed the A face to contain a large anomalous contribution from the linear piezoelectric effect which was absent on the B face (Phys. Rev. Letters, 55, 1323 (1985)).

The remaining phase of our investigation has been a continuing attempt to improve the quality of the ASE measurements so that more reliable data could be obtained. These refinements have included improvement so that more reliable data could be obtained. These refinements have included improvement of the signal to noise ratio of the apparatus, reduction of the time required for data acquisition, improvement in sample control procedures, and development of apparatus and techniques to allow ASE data at elevated temperatures. Good signal to noise is a necessity for accurate lineshape data. Third derivatives of the dielectric constants as a function of energy are required to obtain ASE lineshapes so noise must be kept to a minimum. An improved predispersing system as well as random noise source elimination has allowed lineshape determinations to be practical. Further improvement is being pursued, however. Replacement of the digitally controlled predispersing system with a direct drive predisperser has reduced data acquisition times by nearly a factor of two. This allows more frequent sampling of surfaces and allows less time for surface oxidation of the samples. Sample preparation by surface etching before mounting causes too much opportunity for surface deterioration prior to monitoring. An insitu sample cell capable of allowing surface etching in an

Inert atmosphere immediately prior to data collection has also been developed and allows more reliable values for the dielectric constants to be developed. Finally a hot cell has been built and operated at elevated temperatures. Variations in measured values of the dielectric constants as a function of temperature have been obtained. Still required, however, is the combining in one cell of a heating capability as well as an insitu etching capability. Perfection of such a cell is required before reliable temperature data can be obtained.

## TABLE OF CONTENTS

SECTION	PAGE
LIST OF FIGURES	ii
LIST OF TABLES	iii
EER AND SIMS RESULTS	1
USE OF SPECTROSCOPIC ELLIPSONOMETRY TO STUDY OXIDIZED SURFACES	7
PHYSICAL SIGNIFICANCE OF THE LINEWIDTH $\Gamma$ FOR MERCURY CADMIUM TELLURIDE ALLOYS	10
ASE AND EER RESULTS FOR NVL SAMPLES	11
EER STUDY OF THE A- AND B-FACES OF CdTe	20
IMPROVEMENT OF THE ASE APPARATUS AND CONSTRUCTION OF A HOT CELL	32
STATUS OF THE HOT CELL	38
PRELIMINARY ELLIPSONOMETRIC STUDIES	42
PROPOSED IMPROVEMENTS IN THE HOT CELL	44
REFERENCE LIST	45
SUPPORTED WORK AND RELATED WORK	47
APPENDIX I	49

## LIST OF FIGURES

FIGURE	PAGE
1. SIMS and EER Profiles of the Composition of a Mercury Cadmium Telluride Sample	4
2. Best Fits of Eq. (2) to the ER Signals from the Cd and Te Faces (or A and B Faces) of a CdTe Crystal	26
3. Straight-Line Fits of the Parameters $C_b(\hbar\Omega_b)^3$ and $C_s V_M^{-0.5} \Delta E_s$ as Functions of $V_M$ and $V_M^{0.5}$ , Respectively, Yielded by Eqs. (4) and (5)	30
4. Side View of Cell Showing 2 Windows Only	34
5. Top View of Cell Showing 3 Windows	35
6. Side View of the Heater	36
7. Special Clamps to Mount the Sample and Thermocouple	37
8. Side View of Cell Showing 2 Windows Only	39
9. Top View of Cell Showing 4 Windows	40
10. Side View of the Heater	41
11. Values of $\epsilon_1(\omega)$ and $\epsilon_2(\omega)$ for CdTe from ASE Measurements at Room Temperature and 150 C	43

## LIST OF TABLES

TABLE		PAGE
I.	Application of Ellipsometry to Anodic Oxides	8
II.	VPE #042684(A)	11
III.	VPE #042584(A)	12
IV.	VPE #042584(B)	13
V.	LPE #051084(A)	14
VI.	LPE #050784(A)	15
VII.	LPE #031484(A)	16
VIII.	Values of the Interband Transition Energy E and Broadening Parameter $\Gamma$ for Bulk States (b) and Surface States (s) as Measured by EER on the A and B Faces of CdTe	28



## EER AND SIMS RESULTS

The characterization studies of bulk and epitaxial Mercury Cadmium Telluride by electrolyte electroreflectance (EER)<sup>(1)</sup> and automatic scanning ellipsometry (ASE) that have been undertaken in this investigation covered a number of distinct phases. In the first phase, EER techniques that had proven highly successful in our previous sample composition studies<sup>(2,3)</sup> were extended to study anodic and plasma-deposited oxide layers on MCT samples. These techniques, coupled with SIMS data on the same samples, allowed us to achieve a number of results. Parameters relating to composition, crystal quality, and carrier concentration as a function of depth were measured for oxides deposited on substrates grown by various techniques. These measurements allowed the quality of the semiconductor materials to be compared for various growth procedures and deposition techniques. Crystal damage was found not to be enhanced by oxide deposition but plasma deposition was found to have an effect on Hg depletion within the oxidized region.

Following are summary reports and data for similar plasma oxides grown on  $x = .32$  LPE p-type,  $x = .295$  bulk n-type, and two  $x = .2$  LPE n-type MCT samples. Also included is each sample's detailed descriptive data. Results are given in the format of  $X$  (composition),  $\gamma$  (related to crystal quality), and  $\theta$  (related to carrier concentration).

### Summary:

1. Mercury depletion of the plasma oxidized surface region (first 600Å) appears to be common to all samples except 3b, which was much more defective. (Its linewidth,  $\Gamma$ , was erratic as a function of depth, with an average value of 160 meV). The surface of the bulk sample 2 was shown to be the most impoverished.

Sample			Composition X			Epilayer/Substrate
<u>No.</u>	<u>Variety</u>	<u>Type</u>	<u>Surface</u> <u>(&lt;600Å)</u>	<u>Near Surface</u> <u>(&gt;600Å to 3000Å)</u>	<u>Bulk</u> <u>(&gt;1μm)</u>	<u>Interface Width, μm</u>
* 1	LPE	p	.29	.28	.32	5
2	Bulk	n	.37	.29		-
* 3a	LPE	n	.20	.16	.20-.25	2
* 3b	LPE	n	.14	.18-.20	.20-.22	3

\* Show "usual" Hg enrichment of the surface in LPE materials.

2. Damage at the plasma MCT inter-face appears similar to that throughout the surface region, the first μm. That is,  $\Gamma$  in the surface region is 140 to 170 meV, with a bulk value of 130 meV, except for sample 3b, in which the bulk and surface values are erratic from 140 to 170 meV.

3. Theta with respect to type (0-n type,  $\bar{1}$ -p type).

<u>No.</u>	<u>Sample</u> <u>Variety</u>	<u>Type</u>	<u>Surface</u>	<u>Theta (Radians)</u> <u>Near Surface</u>	<u>Bulk</u>
1	LPE	p	2(type masked)	-----	2.5(masked or tends to p)
2	Bulk	n	†0(n-type)	1.5(type masked)	-----
3a	LPE	n	†0(n-type)	2.2(type masked)	2.5(masked or tends to p)
3b	LP	n	1.5(type masked)	2.2(type masked)	1.5 to 2.7(erratic)

†Seem to have a low enough defect content to exhibit the effects of oxide passivation.

## COMMENTS ON FIGURE 1

- In this figure the S.I.M.S. and EER profile are plotted on a linear scale.
- The sample used was the same in both measurements.
- The material is state of the art T.I. LPE. The top layer, which has a composition of essentially  $x = 0$ , was not removed.
- The peak in the cadmium counts corresponds to the position of the epilayer/substrate interface.
- Notice that the rapid change in composition which takes place around 1.5 microns shows in the S.I.M.S. profile primarily as a rapid change in the mercury counts.
- In this respect the information provided by S.I.M.S. is primarily qualitative but is in excellent agreement with the EER.

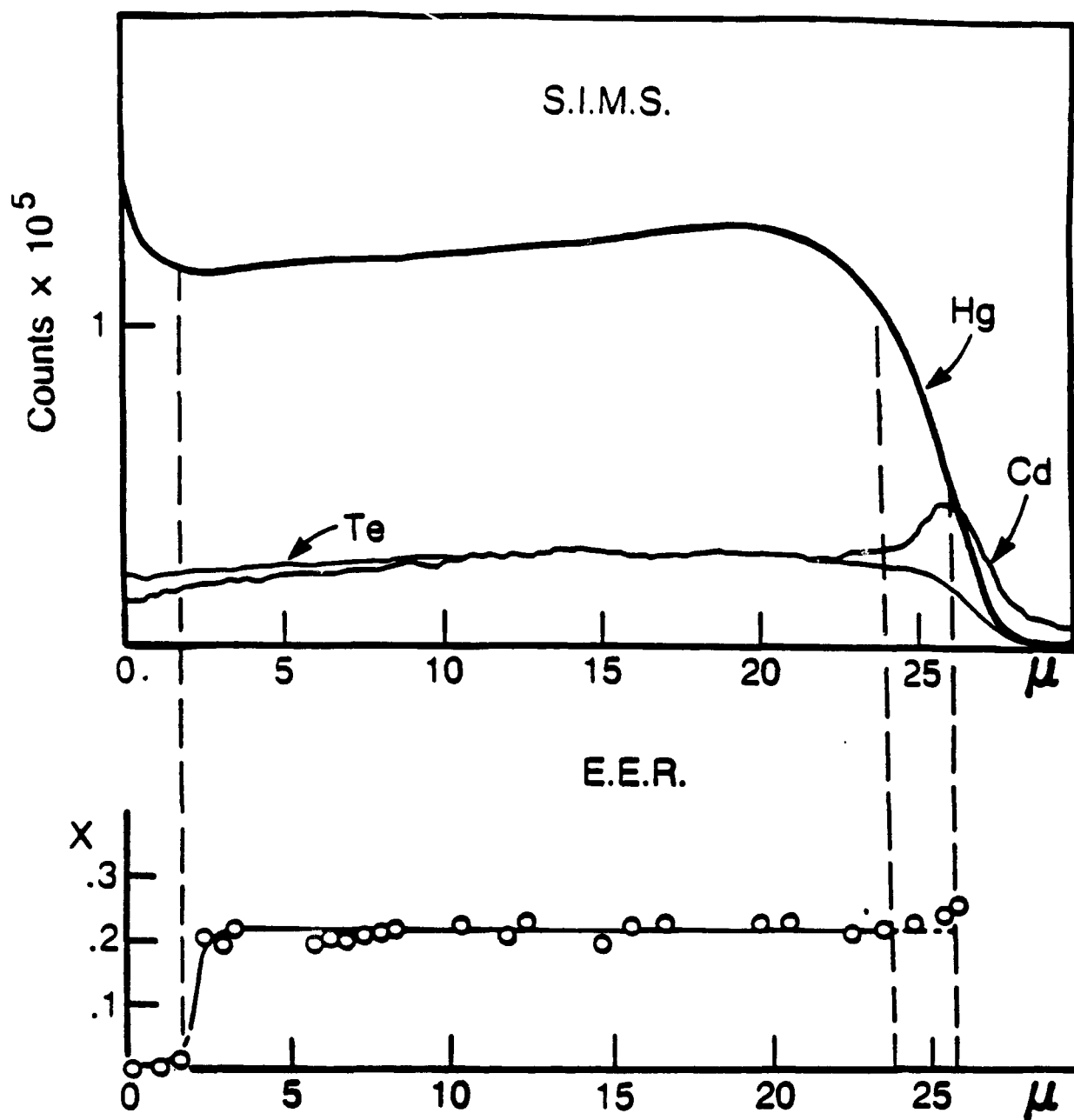


FIGURE 1: SIMS and EER profiles of the composition of a mercury cadmium telluride sample.

### Tentative Conclusions:

Composition: Plasma deposition may induce Hg depletion within the oxidized region.

"Bulk region of LPE sample #1 could be considered state-of-the-art".

"The lateral uniformity of sample #2 was found to be uniform in composition to within  $\pm 0.015$  which is clearly better than the stated  $\pm 0.05$ ".

Damage: "The only thing that can be said is that plasma deposition has not introduced more damage than was already there".

Type: Unambiguous determination of type by EER at room temperature was obtained for samples 2 and 3a only -- perhaps because the effects of charged point defects were masked in EER by the effects of positively charged interfaces.

### SAMPLE DATA

Plasma Conditions: 60 watts RF power  
+40 VDC sample bias  
.5 torr  $O_2$

#### Samples:

#1 488Å Plasma oxide on LPE

6 min. growth time

#5-271B LPE - (111),  $\lambda = 3.87 \mu m$ , 25-28  $\mu m$  thick

p-type,  $4.8 \times 10^{16}/cm^3$  @ 77K

mobility 238  $cm^2 v^{-1} s^{-1}$  @ 77K

$x = .32 \pm .01$  (by EER)

#2 445Å Plasma oxide on Bulk

5 min. growth time

#15(321)-10B - (111), Bulk

n-type,  $-2.7 \times 10^{15}/\text{cm}^3$  @ 300K

$-1.7 \times 10^{14}/\text{cm}^3$  @ 77K

mobility  $5.6 \times 10^3 \text{ cm}^2\text{v}^{-1}\text{s}^{-1}$  @ 300K

$6.4 \times 10^4 \text{ cm}^2\text{v}^{-1}\text{s}^{-1}$  @ 77K

$x = .295 \pm .05$

#3a 237Å Plasma oxide on LPE

2 min. growth time

b 363Å Plasma oxide on LPE

6 min. growth time

#4318 LPE - (111),  $\lambda = 12.5 \mu\text{m}$ ,  $20 \mu\text{m}$  thick

n-type,  $-1.1 \times 10^{14}/\text{cm}^3$  @ 77K

mobility  $1.4 \times 10^5 \text{ cm}^2\text{v}^{-1}\text{s}^{-1}$  @ 77K

$x = .2$

## USE OF SPECTROSCOPIC ELLIPSOMETRY TO STUDY OXIDIZED SURFACES

The second phase of investigation was the extension of our characterization studies to include automatic spectroscopic ellipsometry (ASE). In this phase the effective-medium approximation<sup>(4)</sup> was used to measure the surface roughness at the interface between the oxide and the semiconductor, the fraction of the oxide relative to the semiconductor in the rough interface layer, and the thickness of the oxide. The feasibility of studying the effects of chemical attacks on the surface was thus established.

We began with ellipsometry studies of oxides deposited by anodization. Typical results are summarized in Table I. They show that it is possible to measure the surface roughness at the interface between the oxide and the semiconductor, the fraction of oxide in relation to semiconductor in the rough layer, as well as the thickness of the oxide. It should be noted that the accuracy of this determination is far greater and more dependable than the accuracy of the determination of the oxide thickness made by single wavelength ellipsometry. The reason is that no assumptions are made here as to the optical properties of the oxide or of the semiconducting substrate since both can be measured separately.

The results show that it is possible to study the effects of different chemical attacks on the surface. An example of the study of the surface after removal of the oxide is given for illustration. One sees that a lactic acid dissolution of a 256Å oxide layer leaves behind a 9Å layer of native oxide coating the original interface layer, the thickness of which is almost unchanged (12Å, as compared to 15Å).

TABLE I

APPLICATION OF ELLIPSOMETRY  
TO ANODIC OXIDES

	OX	F	DR	N
#1 With Oxide	256Å	35	15Å	2.24
Oxide Removed	9Å	33	12Å	2.21
#2 With Oxide	554Å	36	15Å	2.28

OX = OXIDE THICKNESS

F = VOLUME FRACTION OF OXIDE IN THE INTERFACE REGION

DR = THICKNESS OF THE INTERFACE REGION

N = INDEX OF REFRACTION OF THE OXIDE BELOW THE OPTICAL GAP



Much effort was devoted to the installation of two predisperser systems on the ellipsometer, as well as to the elimination of systematic and random noise.

## RESULTS

- A) A grating predisperser which has been installed and is driven by the computer, reduces by 4 orders of magnitude the scattered light in the system, thereby permitting greater accuracy in the higher photon energy range.
- B) A prism predispersing system, which also has been installed, allows us to eliminate higher orders and therefore spares us the need to use automatic filter positioning.
- C) A systematic tracking of all random noise sources has allowed us to improve the signal-to-noise ratio by a factor of two thereby making it easier to carry out first, second and third numerical derivatives of the experimental signal.

PHYSICAL SIGNIFICANCE OF THE LINEWIDTH  $\Gamma$  FOR MERCURY CADMIUM TELLURIDE ALLOYS

We studied the physical significance of the parameter  $\Gamma$ , which can be obtained by electrolyte electroreflectance (EER) or by spectroscopic ellipsometry.

The generalized theory of electroreflectance<sup>(5,6)</sup> (which has been carried out under separate funding) has permitted us to reconcile the  $\Gamma$  obtained by electroreflectance to the  $\Gamma$  obtained by ellipsometry. However, the value of  $\Gamma$  obtained either way can be as high as 120 meV, as compared to the expected 70 meV. We have determined that this is due to the breakdown of the virtual crystal assumption and is in fact a quantitative measure of it. It turns out that the measured value of  $\Gamma$  is approximately given by  $\Gamma_m = [\Gamma_0^2 + (\Delta\Gamma)^2]^{0.5}$ , where  $\Gamma_m$  is the measured linewidth,  $\Gamma_0$  is the expected 70 meV, and  $\Delta\Gamma$  measures the departure from the virtual crystal approximation. (See Appendix I)

## ASE AND EER RESULTS FOR NVL SAMPLES

We also studied 7 samples provided by Night Vision Laboratories (See Tables II-VII). We have addressed the question of growth on A versus growth on B surfaces and found that the differences are clear. We have addressed as well the question of comparison between layers grown by LPE versus layers grown by VPE. Here again we have seen what we have reported before,<sup>(3,7)</sup> namely, that VPE layers are graded in composition and we have now established that this grading is accompanied by extensive strains. In comparison layers grown by LPE are superior.

LPE

## Comments on Material Results:

1. The surfaces of samples #051084(A), #031484(A) and #050784(A) are Hg rich. In general, the composition profiles are flat with a 4  $\mu$ m inter-diffusion width.
2. The 20 min. longer growth time of #050784(A) relative to #051084(A) has resulted in a 6  $\mu$ m thicker layer with an x value approx. 0.02 less than that for #051084(A). Other growth parameters were reported as similar.
3. The one gram larger melt weights, different furnace, and higher (513°C vs. 497°C) ranged (.2°C/min.) temperature vs. fixed temperature between samples #031484(A) and #051084(A) has resulted in a decrease in the x value of approx. 0.04 for #031484(A) and an increase of 2  $\mu$ m in thickness. Other growth parameters, duration, environment, etc., were reported as similar.

## Comments on Analysis:

In general, EER and ASE agree well for all LPE samples.

TABLE II  
VPE #042684(A)

DEPTH IN MICRONS	E <sub>1</sub>		X	$\Gamma$	$\theta$	$\Delta_1$	$\Delta\sigma^2$
	EER	ASE	EER	EER	EER		
0.0	2.330	2.324	0.256	0.115	4.382	- 8.351	- 6.624
0.53	2.336	2.332	0.262	0.084	3.771	-79.986	-16.852
1.05	2.338		0.264	0.103	4.238	-10.444	- 3.584
1.57	2.343	2.340	0.269	0.103	4.217	- 9.519	- 3.202
2.10	2.343	2.347	0.269	0.102	4.223	-10.482	- 3.276
2.63	2.349	2.347	0.276	0.105	4.183	-12.394	- 3.897
3.15	2.355	2.358	0.282	0.106	4.268	- 9.586	- 3.153
3.68	2.360	2.359	0.287	0.103	4.214	-10.539	- 3.205
4.21	2.364	2.360	0.291	0.099	4.146	-24.579	- 5.481
4.73	2.364	2.365	0.291	0.106	4.357	- 9.637	- 2.226
5.26	2.387	2.369	0.315	0.106	4.497	- 4.-15	- 2.705
5.78	2.372	2.372	0.299	0.110	4.300	- 9.545	- 2.421
6.31	2.375	2.375	0.302	0.101	4.174	-16.254	- 3.649
6.84	2.382	2.381	0.310	0.108	4.216	-12.545	- 3.291
7.36	2.389	2.390	0.316	0.110	4.277	-11.563	- 2.409
7.89	2.404	2.404	0.331	0.105	4.240	-13.190	- 3.209
8.74	2.432	2.433	0.358	0.111	4.282	-13.287	- 2.959
9.58	2.445	2.440	0.370	0.110	4.308	-13.760	- 3.037
10.42	2.459	2.450	0.383	0.110	4.278	-16.170	- 3.333
11.26	2.469	2.461	0.393	0.113	4.247	-17.882	- 3.447
12.10	2.490	2.477	0.411	0.121	4.604	- 6.673	- 2.670
12.94	2.547	2.547	0.460	0.139	4.893	- 6.253	- 2.815
14.21	2.585		0.492	0.152	4.893	- 7.107	- 3.303
15.47	2.637	2.610	0.533	0.188	5.095	- 7.241	- 3.773
16.73		2.729					

TABLE III  
VPE #042584(A)

DEPTH IN MICRONS	EER	$E_1$ ASE	X EER	$\Gamma$ EER	$\theta$ EER	$\Delta_1$	$\Delta\sigma^2$
0.0	2.398	2.359	0.325	0.102	5.917	34.951	- 0.216
0.48	2.384	2.373	0.312	0.106	4.138	-15.045	- 3.586
0.95	2.399	2.377	0.326	0.113	4.492	- 6.171	- 3.056
1.43	2.405		0.332	0.104	4.245	-13.469	- 3.811
1.90	2.419	2.402	0.346	0.112	4.559	- 4.358	- 3.291
2.38	2.419	2.406	0.346	0.104	4.114	-20.869	- 5.194
2.85	2.424	2.410	0.351	0.104	4.213	-20.358	- 5.004
3.33	2.435	2.424	0.351	0.109	4.313	-13.119	- 3.632
3.81	2.440	2.430	0.365	0.106	4.160	-19.369	- 4.461
4.29	2.445	2.435	0.371	0.108	4.157	-21.594	- 4.590
4.76	2.478	2.444	0.400	0.124	4.632	- 2.587	- 3.193
5.24	2.459	2.447	0.383	0.107	4.073	-22.306	- 4.361
5.71	2.491	2.466	0.394	0.128	4.302	-33.463	- 5.395
6.19	2.487	2.474	0.409	0.160	4.757	- 6.959	- 1.207
6.67	2.502	2.498	0.422	0.122	4.214	-15.984	- 2.722
7.14	2.529	2.526	0.445	0.133	4.413	-18.058	- 2.571
7.90	2.539	2.534	0.454	0.107	4.033	-41.850	- 5.147
8.67	2.553	3.554	0.466	0.113	4.035	-33.686	- 3.889
9.43	2.572	2.577	0.482	0.123	4.127	-28.224	- 3.074
10.19	2.670	2.601	0.559	0.163	0.105	10.879	- 0.548
10.95	2.652	2.605	0.545	0.201	0.310	4.405	- 0.073
11.71	2.637	2.700	0.533	0.249	5.160	- 4.639	- 1.051
12.86	2.691	2.793	0.575	0.297	4.974	- 4.354	- 0.916
15.14	3.375		1.00	0.130	0.843	5.292	0.694

TABLE IV  
VPE #042584(B)

DEPTH IN MICRONS	EER	$E_1$ ASE	X EER	$\Gamma$ EER	$\theta$ EER	$\Delta_1$	$\Delta\sigma^2$
0.0	2.347	2.331	0.274	0.097	5.293	-57.775	4.892
0.48	2.351	2.330	0.278	0.125	5.177	-23.905	2.557
0.95	2.352	2.343	0.279	0.101	5.215	-32.016	3.309
1.43	2.362		0.289	0.102	5.174	-24.977	3.211
1.90	2.360	2.347	0.287	0.102	5.186	-29.196	3.392
2.38	2.367	2.354	0.294	0.102	5.136	-24.400	3.337
2.85	2.376		0.303	0.101	5.145	-25.937	3.568
3.33	2.378	2.362	0.306	0.102	5.175	-26.329	3.141
3.81	2.378	2.369	0.305	0.096	5.212	-29.958	3.187
4.29	2.394	2.377	0.321	0.105	5.176	-29.663	3.195
4.76	2.406	2.378	0.333	0.083	5.517	-77.702	6.705
5.24	2.401	2.378	0.328	0.102	5.180	-35.096	3.490
5.71	2.407	2.393	0.334	0.109	5.151	-29.246	3.003
6.19	2.418	2.401	0.345	0.106	5.125	-29.674	3.206
6.67	2.426	2.416	0.352	0.125	5.103	-28.216	2.732
7.14	2.423	2.420	0.350	0.112	5.027	-23.246	3.101
7.90	2.440	2.428	0.365	0.109	5.095	-25.279	3.779
8.67	2.450	2.437	0.377	0.116	5.041	-20.570	3.260
9.43	2.467	2.456	0.390	0.145	5.026	-18.006	1.730
10.19	2.479	2.469	0.402	0.131	4.989	-17.933	2.624
10.95	2.504	2.496	0.423	0.125	5.100	-24.235	3.138
11.17	2.590	2.581	0.496	0.160	5.311	-18.106	1.662
12.86	2.745	2.710	0.614	0.152	5.432	-29.389	2.944

TABLE V  
LPE #051084(A)

DEPTH IN MICRONS	$E_1$ EER	ASE	X EER	$\Gamma$ EER	$\theta$ EER	$\Delta_1$	$\Delta\sigma^2$
0.0	2.341	2.449	0.267	0.098	4.198	-19.270	-10.115
1.375	2.404	2.397	0.331	0.114	4.394	-16.765	- 4.788
2.750	2.399	2.393	0.327	0.110	4.489	-13.142	- 4.392
4.125	2.390	2.395	0.318	0.101	4.321	-24.993	- 5.755
5.500	2.397	2.399	0.324	0.111	4.491	- 9.604	- 3.582
6.875	2.406	2.399	0.333	0.108	4.439	-12.232	- 2.506
8.250	2.437		0.363	0.129	4.894	2.392	- 4.039
9.625	2.544	2.519	0.458	0.189	5.977	4.005	- 0.771

TABLE VI  
LPE #050784(A)

DEPTH IN MICRONS	EER	$E_1$ ASE	X EER	$\Gamma$ EER	$\theta$ EER	$\Delta_1$	$\Delta\sigma^2$
0.0	2.260	2.268	0.176	0.088	4.138	-25.166	- 9.760
1.35	2.378	2.366	0.306	0.109	4.546	- 8.889	- 3.223
2.70	2.370	2.366	0.297	0.110	4.484	-10.236	- 3.460
4.04	2.369	2.360	0.296	0.108	4.565	- 9.470	- 3.795
5.38	2.365	2.361	0.292	0.105	4.580	- 7.646	- 3.353
6.73	2.362	2.356	0.289	0.103	4.563	- 7.756	- 3.246
8.08	2.361	2.352	0.288	0.113	4.871	0.042	- 3.529
9.42	2.357	2.355	0.284	0.102	4.469	- 7.076	- 3.314
10.77	2.354	2.355	0.281	0.097	4.382	-11.906	- 3.490
12.12	2.359	2.361	0.286	0.099	4.377	-12.177	- 3.591
13.46	2.379	2.384	0.307	0.101	4.430	-15.780	- 3.784
14.81	2.419	2.461	0.345	0.113	4.550	-21.923	- 4.872
16.15	2.508		0.427	0.181	4.855	- 8.956	- 4.574
17.50			0.995				



TABLE VII  
LPE #031484(A)

DEPTH IN MICRONS	$E_1$ EER	ASE	X EER	$\Gamma$ EER	$\theta$ EER	$\Delta_1$	$\Delta\sigma^2$
0.0	2.212	2.230	0.115	0.098	4.136	- 8.196	- 4.490
1.35	2.358	2.352	0.285	0.114	4.569	- 8.443	- 3.272
2.70	2.353	2.351	0.279	0.106	4.383	- 7.251	- 2.656
4.05	2.351	2.349	0.278	0.111	4.531	- 5.938	- 2.285
5.40	2.355	2.355	0.282	0.107	4.439	- 7.653	- 2.543
6.75	2.360	2.353	0.287	0.108	4.451	- 7.704	- 2.776
8.10	2.366		0.293	0.106	4.387	- 8.231	- 2.686
9.45	2.397	2.383	0.325	0.108	4.368	-10.928	- 3.063
10.80	2.458	2.439	0.382	0.123	4.421	-13.524	- 2.778
12.15	2.570	2.544	0.480	0.215	4.611	-12.095	- 2.333
13.5			0.993				

VPE

## Comments on Materials Results:

1. Epilayers are graded showing an  $x$  variation of approx. 0.15 within the more slowly varying first 11  $\mu\text{m}$  of depth.
2. Samples #042584(A) and #042584(B) show the effect of the different growth faces, with the 0-11  $\mu\text{m}$  region of the B face growth, #042584(B), having an  $x$  value approx. 0.05 less than that of the A face growth, #042584(A). As both appear equal in thickness and growth parameters, this may indicate a reduced out-diffusion of Cd for the B face growth.
3. The  $x$  value of #042684(A) is less than that of #042584(A) by approx. 0.075 to 0.12. This appears to show an effect of the  $\text{H}_2$  pressure [600 psi for #042584(A) and 750 psi for #042684(A)] as other reported growth parameters were similar.

## Comments on Analysis:

In general the EER and ASE profiles agree well; however there is some disagreement at several points. A check against reflectance data finds ASE and reflectance in agreement except for an absolute shift in  $x$  (or  $E_1$ ), probably due to a small calibration difference. That is, the few larger variations in composition shown by EER are not present in the ASE or reflectance results.

The first two phases provided the impetus for the crucial third phase of study which involved unifying the EER and ASE measurements. A study of 7 NVL samples by both techniques revealed like results from measurements of the  $E_1$  energies, with the best agreement recorded for LPE samples. Linewidth data,

however, which is related to crystal quality differs for the two techniques. Comparative lineshape measurements from EER and ASE allowed the development of a generalized theory of EER<sup>(5,6)</sup> and a newly proposed expression for the EER lineshape. Since electrostriction and defect polarization are included in the generalized theory, the anomalous lineshapes observed provided a measure of long range strain and defect polarizability. This generalized theory exhibited its potential when EER was used to study the A and B faces of CdTe and revealed the A face to contain a large anomalous contribution from the linear piezoelectric effect which was absent on the B face.

## EER STUDY OF THE A- AND B-FACES OF CdTe

We now report the results of a comparative study of the A and B polar (111) faces of CdTe using electrolyte electroreflectance (EER). Even though the use of an ambient technique such as EER to study CdTe makes inescapable the presence of a native oxide layer which inhibits surface reconstruction, a giant local piezoelectric contribution to the A-face signal was observed, whereas the B-face signal contained no such contribution. A large signal of the type which we have observed from the A-face of CdTe can arise only from unusually large-electric-field-driven local distortions on or near that surface, i.e., only from a large local piezoelectric effect. Therefore, we must conclude that there exists a region of greatly lowered stability associated with the oxidized A-face but not with the oxidized B-face, which exhibits no such signal. We interpret this lowered stability as arising from bond bending at the A-interface between the CdTe and its native oxidized surface film. As is shown in detail in this communication, a careful analysis of the data imposes that the observed giant piezoelectric signal arises primarily from a two-dimensional interfacial region having a thickness of no more than two or three atomic layers.

We believe these striking results to be related to differences between the reconstruction of the clean A-face of CdTe and that of the clean B-face. It is well known both experimentally<sup>(8)</sup> and theoretically<sup>(9)</sup> that the reconstruction of the clean A-face of zincblende materials differs substantially from that of the clean B-face. In particular, the A-face reconstruction involves a much greater lowering of the energy; thus it is more difficult for an oxide film to totally

inhibit the reconstruction of the A-face. Also, the A-face reconstruction involves the formation of a large number of cation vacancies<sup>(8-11)</sup> which would remain after oxidation, whereas the B-face reconstruction does not.<sup>(8-10)</sup>

Recently, we have generalized the electroreflectance (ER) theory of Aspnes<sup>(12)</sup> to account quantitatively for the effects of piezoelectricity, strain, polarizable defects and alloy disorder (where applicable). Our results show that piezoelectric shifts as small as  $10^{-4}$  eV in either local or bulk interband transition energies give rise to ER signals not previously understood. These signals, which were observed<sup>(13)</sup> as early as 1966, have a lineshape substantially different from that of the usual ER lineshape<sup>(12)</sup> and in the absence of inversion symmetry also have a different dependence on the modulating electric field  $\vec{E}_M$ . This effect is greatly enhanced by the existence of lowered structural stability, such as that expected at the A-face of CdTe. In the absence of this effect, because the light penetration in the energy range of interest is at least of order  $100\text{\AA}$  one would expect the ER lineshape to contain only a very small contribution from the interface region. However, our theory suggests that a marked lowering of the structural stability at the A-face interface could lead to an electrostrictive polarizability large enough to allow one to sample the two-dimensional interface region independently of the bulk, even though it occupies only a small fraction of the total volume probed.

Our experimental results have confirmed this suggestion in a spectacular manner. For the same crystals we found very similar bulk EER signals from the A- and B-faces but found the A-faces to exhibit a large additional linear piezoelectric signal at a somewhat higher critical energy. We have confirmed the nature of this additional signal by lineshape analysis and by a study of its dependence on  $E_M$ . The EER system, which is described elsewhere,<sup>(14)</sup> was used

to obtain spectra in the vicinity of the  $E_1$  critical point from (111) oriented CdTe samples.

Typical EER spectra obtained from A- and B-faces of the same sample are shown in Fig. 2; the difference between the two lineshapes is obvious. This difference is independent of the electrolyte used (organic or 1/10 N KOM or 1/5N lactic acid) and was observed for all of our single-crystal samples. These samples were of varied origin and were grown by different methods. The quantitative results discussed here were obtained from a sample carefully selected to be of exceptional structural quality which was given a careful chemomechanical bromine/methanol polish to produce relatively damage-free surfaces. This treatment is standard for CdTe wafers prior to epitaxial HgCdTe growth. Both A-and B-faces are easily polished and epitaxial layers can be grown on both types of surfaces.

EER spectra were obtained at six different modulation voltages from 5V to 30V in order to analyze the dependence on  $E_M$  of the amplitudes of the various contributions to the total lineshape. In addition, automatic spectroscopic ellipsometry (ASE) was used to determine the optical properties of both the Cd and the Te faces, and the third-derivative spectra were numerically computed and compared to the EER results.

For any derivative spectroscopy, such as ER, the lineshape arises primarily from interband transitions in the immediate vicinity of critical points in the Brillouin zone. In general, the contribution of a given interband transition and given critical point to the low-field ER lineshape is given by the expression,

$$L_j(E) = A(-\Delta E_j D_j^{(1)}(E) + [\Delta\sigma^2 + 1/2(\Delta E_j)^2] D_j^{(2)}(E) + 1/3(\hbar\Omega_j)^3 D_j^{(3)}(E)). \quad (1)$$

Here,  $A$  is a constant independent of the modulating field  $\tilde{E}_M$ ,  $\Delta E_j$  and  $\Delta\sigma^2$  are the shifts due to  $\tilde{E}_M$  in the critical-point interband transition energy  $E_j$  and in

the mean-squared scattering potential  $\sigma^2$  from defects and/or alloy disorder, respectively, and  $\hbar\Omega_j$  is the energy gained from the field  $\hat{E}_M$  by the optically excited carriers. The term quadratic in  $\Delta E_j$ , which is negligible in most cases, is included because  $\Delta E_j$  is expected to be unusually large for the A-face, whereas  $\Delta\sigma^2$  is expected to be relatively small. The functions  $D_j^{(m)}(E)$  are given by the equations

$$D_j^{(m)}(E) = E^{-2} \left[ \alpha \frac{\partial^m E^2 \epsilon_{1j}}{\partial E^m} + \beta \frac{\partial^m E^2 \epsilon_{2j}}{\partial E^m} \right],$$

where  $\alpha$  and  $\beta$  are the Seraphin coefficients<sup>(15)</sup> and  $\epsilon_{1j}$  and  $\epsilon_{2j}$  are the real and imaginary parts of that part of the dielectric function which arises from the given interband transition in the vicinity of the given critical point. Note that  $\Delta E_j$  and  $\Delta\sigma^2$  contain parts linear in  $\hat{E}_M$  for any crystal not having inversion symmetry and for surface effects, whereas  $(\hbar\Omega_j)^3$  is strictly quadratic in  $\hat{E}_M$ .

For the  $E_1$  critical point, which for CdTe has dimensionality  $d=2$ , upon making the usual approximations,<sup>(5,6)</sup> Eq. (1) reduces to the closed form

$$L_1(E) = C \left( -\frac{3}{2} [\Delta E_1 L_1^{(1)}(E) + (2\Delta\sigma^2 + (\Delta E_1)^2) L_1^{(2)}(E)] + (\hbar\Omega_1)^3 L_1^{(3)}(E) \right). \quad (2)$$

Here  $C$  is another constant independent of  $\hat{E}_M$ , and

$$L_1^{(m)}(E) = \cos(\theta_1 - m\phi_1) / [(E - E_1)^2 + \Gamma_1^2]^{m/2}, \quad (3)$$

where  $\theta_1$  is a phase angle which is treated as a parameter,  $\Gamma_1$  is a phenomenological broadening parameter, and  $\phi_1$  is given by the expression

$$\phi_1 = \tan^{-1} [\Gamma_1 / (E - E_1)].$$

Both Eqs. (1) and (2) reduce to the corresponding Franz-Keldysh results of Aspnes<sup>(12)</sup> for the case in which  $\Delta E_j = \Delta \sigma^2 = 0$ .

The final expression used to fit our EER data was obtained by substituting Eq. (3) into Eq. (2) and allowing an adjustable constant background, which is assumed to arise from any surface film present and/or from the tails of signals from critical points distant in energy. The quantities  $C\Delta E_1$ ,  $C\Delta \sigma^2$ ,  $C(\hbar\Omega_1)^3$ ,  $\theta_1$ ,  $E_1$  and  $\Gamma_1$  usually are treated as free parameters, although  $E_1$  and  $\Gamma_1$  could have been determined from ASE and held fixed.

The B-face lineshape contained only a negligible first-derivative term and a small second-derivative term and could be well fit in terms of a single transition between bulk states in the vicinity of a single critical point. On the other hand, the A-face spectra contained a large first-derivative contribution associated with a giant electrostrictive polarizability on that face and a substantial second-derivative term in addition to the usual third-derivative Franz-Keldysh term.

In considering the physical interpretation of these results we must examine the implications of the fact that our measurement was not made in vacuum and therefore that both surfaces of the crystal were covered by a native oxide. Our ASE measurements and others<sup>(16)</sup> show that such oxide layers grow only two or three atomic layers ( $\sim 7$  Å) in the period of time after etching during which we carry out our measurements. Their spectra are featureless in the spectral region of interest and make no observable contribution to the EER signal; moreover, the difference between the A- and B-face signals is unaffected by the thickness of the native oxide (at most 30 Å). Therefore, the semiconductor/oxide interface on the A-face must differ markedly from that on the B-face, and the large magni-



of the additional first-derivative A-face signal must arise from a large linear electrostrictive polarizability associated with the A interface.

In order to test whether the large first-derivative contribution to the A-face lineshape arises from the interface region or from the bulk, we attempted first to fit the A-face lineshape in terms of a single transition between bulk states. Somewhat to our surprise, we found a reasonable fit, although the data displayed a small asymmetry not reproduced well by the fit. In this fit we found  $\Delta\sigma^2$  to be comparable for the two faces but found  $\Delta E_1$  to be large for the A-face. However, we found  $E_1$  to be 25 meV higher and  $\Gamma_1$  to be 25 meV smaller for the A-face than for the B-face, showing the fit and hence the assumption of a single bulk transition to be incorrect for the A-face. This conclusion was confirmed by comparison with ASE, which showed the  $E_1$  value to be correct for the B-face but not for the A-face. Also, the B-face lineshape could be fit after being numerically differentiated, but the A-face lineshape could not be. Thus, the first-derivative piezoelectric signal must arise from different transitions than those which give rise to the bulk third-derivative signal. Those transitions must be confined to a region near the A-face with depth considerably less than the depth of light penetration.

Having established that the first-derivative signal arises from an interfacial region which includes no more than one layer of oxide and does not reach far into the bulk, we then addressed the question, "Does that region include only one or two atomic layers or does it extend several atomic layers into the bulk?" In order to answer this question we fit the A-face data as the sum of two lineshapes - one from the bulk having no first-derivative (piezoelectric) term and one from the interfacial region having no third-derivative term. Second-derivative terms, which result from polarizable defects, were allowed in both line-

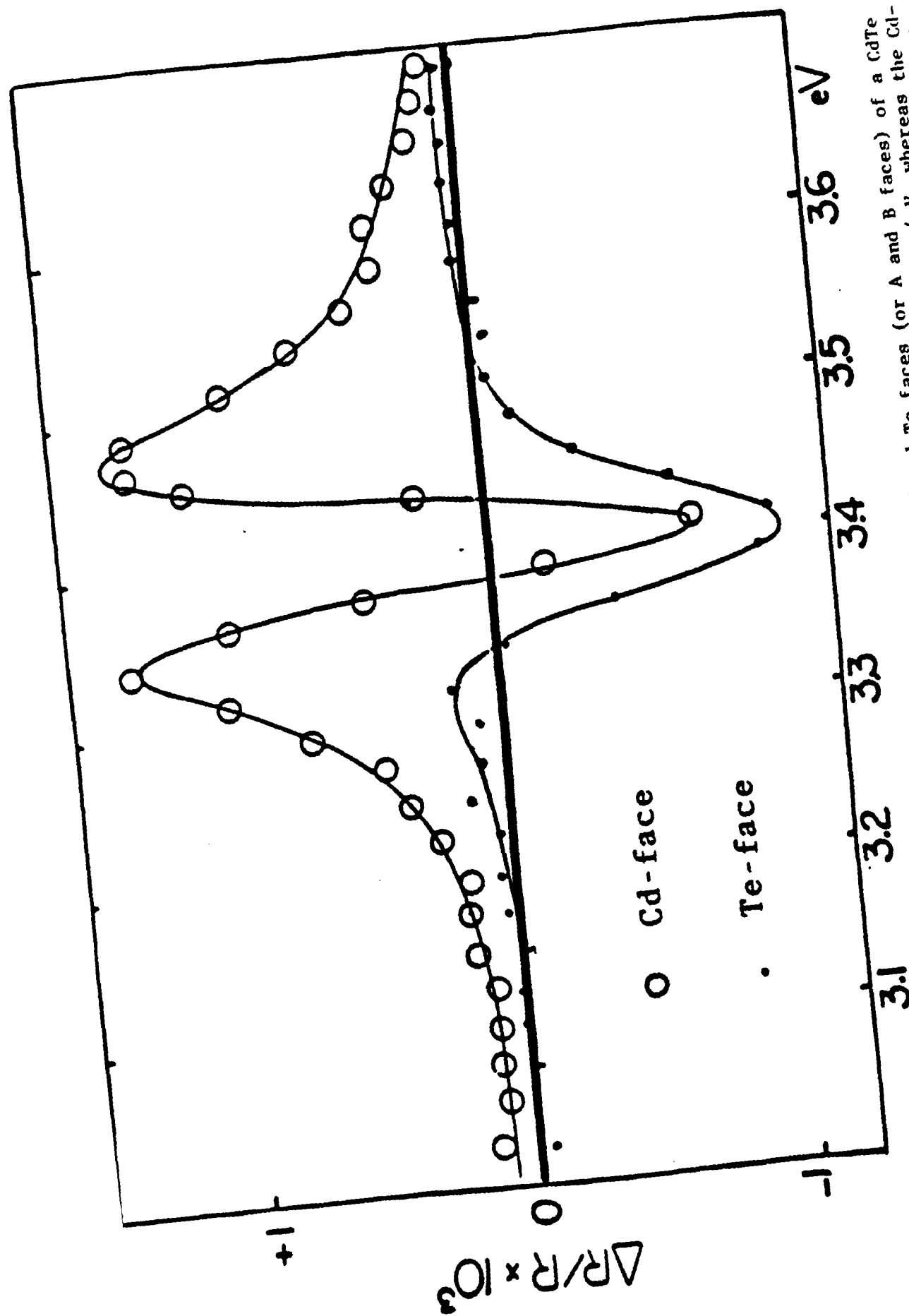


FIGURE 2: Best fits of Eq. (2) to the ER signals from the Cd and Te faces (or A and B faces) of a CdTe crystal. The Te-face signal was obtained with a modulation voltage  $V_M = 4$  V, whereas the Cd-face signal was obtained with  $V_M = 30$  V. Thus, the Te-face signal is a factor of 7.5 smaller than the third-derivative component of the Cd-face signal which digs a sharp hole in the positive first-derivative piezoelectric component.

shapes. Because the two lineshapes had been shown to arise from different regions of the crystal, we allowed all parameters to vary independently for each of them. Best fits to the data for both faces are shown in Fig. 2, and values of the significant field-independent parameters obtained from those fits are shown in Table VIII. The bulk values found for  $E_1$  were essentially the same for the A- and B-faces, but the first-derivative signal from the interfacial region gave a transition energy larger by -44 meV and a broadening parameter of only -60 meV, smaller than the A-face bulk value by -33%. If the interfacial region extended several atomic layers into the bulk, the transition energy would vary smoothly as a function of depth, leading to an inhomogeneous broadening of the first-derivative signal, contrary to what is seen. Thus, the first-derivative piezoelectric signal must arise from an interfacial region having a thickness of no more than one or two atomic layers. The origin of the observed narrowing of the lineshape in the interfacial region is not clear; it could arise from a different atomic structure at the interface. The best fits also give a value of  $\Delta\sigma^2$  for the A-face bulk lineshape approximately three times as large as that for the B-face lineshape. We attribute this result at least in part to the effect of vacancies associated with the original A-face reconstruction which remained after oxidation.

In order further to check the validity of our model for the observed A-face lineshape, we determined the dependence of the parameters  $(M\Omega_b)^3$ ,  $\Delta E_s$ ,  $(\Delta\sigma^2)_b$  and  $2(\Delta\sigma^2)_s + (\Delta E_s)^2$  on the modulation voltage  $V_M$ , which according to the Schottky barrier theory is proportional to  $E_M^2$ . (Here, the subscripts s and b denote surface and bulk values, respectively). We found the following results

TABLE VIII

VALUES OF THE INTERBAND TRANSITION ENERGY  $E$  AND BROADENING  
PARAMETER  $\Gamma$  FOR BULK STATES (b) AND SURFACE STATES (s) AS  
MEASURED BY EER ON THE A AND B FACES OF CdTe.

	$E_b$ (eV)	$\Gamma_b$ (eV)	$E_s$ (eV)	$\Gamma_s$ (eV)
A-face	$3.388 \pm 0.006$	$0.092 \pm 0.006$	$3.432 \pm 0.006$	$0.062 \pm 0.006$
B-face	$3.379 \pm 0.005$	$0.075 \pm 0.005$	...	...

in agreement with theory, which predicts that  $(\kappa\Omega_b)^3$  is proportional to  $V_M$  and that  $\Delta E$  and  $\Delta\sigma^2$  both must be of the form  $aV_M^{0.5} + bV_M$ :

$$C_b (\kappa\Omega_b)^3 = 0.0574 V_M, \quad (4)$$

$$C_s \Delta E_s = -17.29 V_M^{0.5} + 0.38 V_M, \quad (5)$$

$$C_b (\Delta\sigma^2)_b = 0.71 V_M^{0.5} - 0.043 V_M, \quad (6)$$

$$C_s (\Delta\sigma^2)_s = 0, \text{ and} \quad (7)$$

$$C_s (\Delta E_s)^2 = (C_s \Delta E_s)^2 / C_s = 0.1724 V_M. \quad (8)$$

Here,  $\kappa\Omega$ ,  $E_s$  and  $\sigma$  are measured in units of electron-volts, and  $V_M$  is measured in volts. From Eqs. (5) and (8) we find  $C_s = 1.7 \times 10^3$  and thus find

$$\Delta E_s = -0.01 (V_M^{0.5} - 0.02 V_M).$$

The fits of  $C_b(\kappa\Omega_b)^3$  and  $C_s\Delta E_s$  to Eqs. (4) and (5) are shown in Fig. 3. The relative scatter in the fits to Eqs. (6) and (8) are larger by a factor of about two because the quantities being fit are much smaller. If we assume  $(\kappa\Omega_b)^3 = 3 \times 10^{-6} V_M$ , which is consistent with estimates of Aspnes,<sup>(17)</sup> we find  $C_b = 2 \times 10^7$  or  $|C_s/C_b| = 0.08$ . This result is reasonable because the ratio  $C_s/C_b$  should be of the same order as the ratio of the thickness of the interfacial region to the depth of light penetration.

Although our results say nothing quantitative about the structure of the A-face CdTe/oxide interface, the following possible model for the interface suggests itself. On the A-face the interface is between a Cd-face and the oxide matrix, whereas on the B-face it is between a Te-face and the oxide matrix.

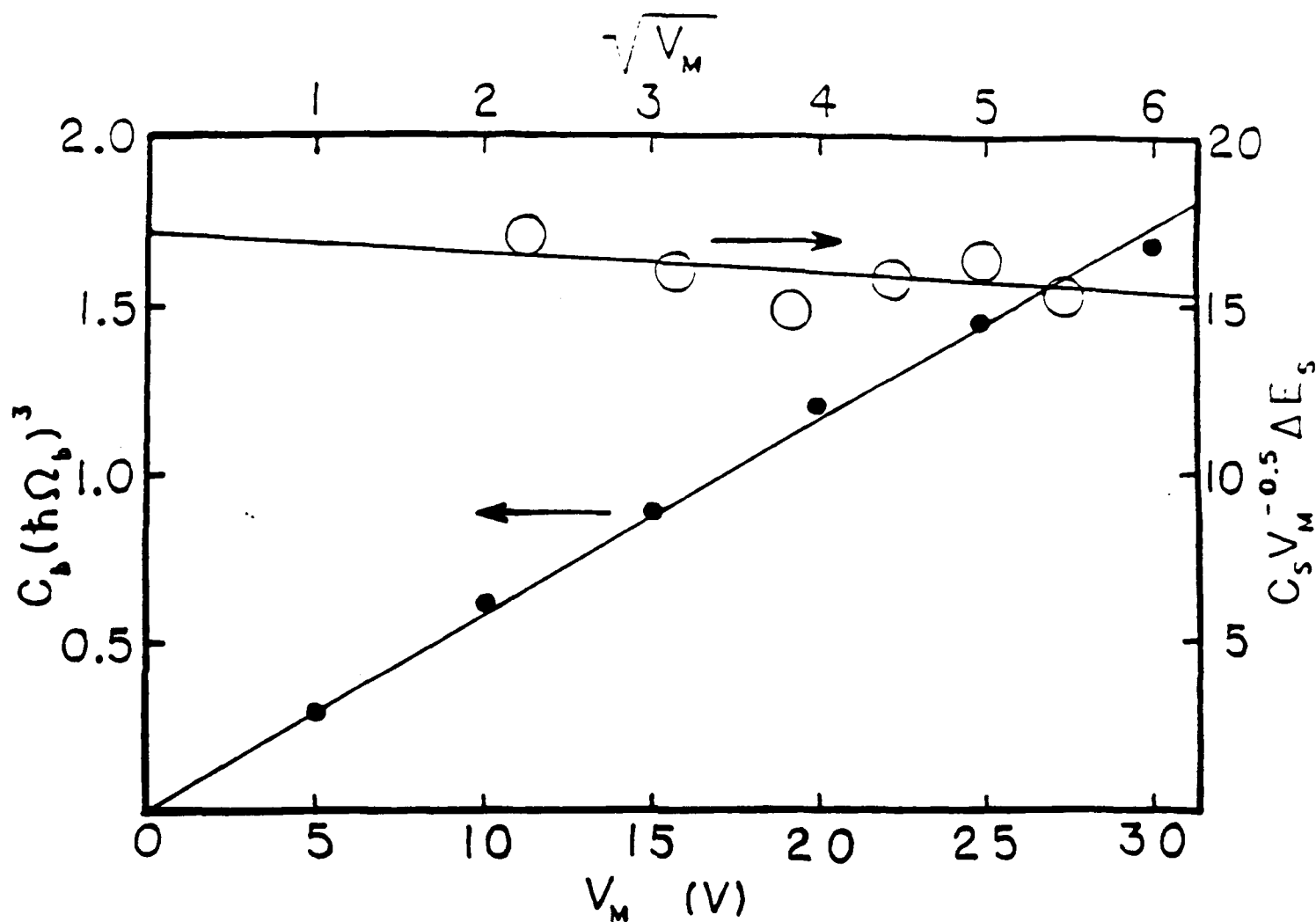


FIGURE 3: Straight-line fits of the parameters  $C_b(h\Omega_b)^3$  and  $C_s V_M^{-0.5} \Delta E_s$  as functions of  $V_M$  and  $V_M^{0.5}$ , respectively, yielded by Eqs. (4) and (5).

matrix. There is no reason to expect the oxide to destabilize the Te-face, the reconstruction of which does not involve vacancy formation. However, it is conceivable that oxygen atoms in the first monolayer bond with the Cd-face, more or less as Te atoms would, giving a sort of epitaxy between the CdTe and the oxide and inhibiting the reconstruction observed on clean Cd faces. This would explain the observed disappearance of the Cd-face reconstruction upon oxidation. However, due to the Cd vacancy formation which accompanies the original reconstruction, it would allow large strains and a high polarizability at the interface. The additional A-face signal would then come from a highly polarizable two dimensional Cd(Te,O) crystal residing at the interface between the CdTe A-face and the native oxide. We summarize our results as follows.

We have found that the electroreflectance spectrum of the (111) A-face of CdTe contains a large anomalous contribution from the linear piezoelectric effect, which is absent on the B-face. We interpret this contribution as arising from electronic transitions occurring in the two-dimensional A-face CdTe/oxide interfacial region, verifying this interpretation by using our generalized theory<sup>(5,6)</sup> of electroreflectance to perform a detailed analysis of our EER spectra, including their field dependence. We also offer a model for the structure of this interfacial region. The critical energy and other quantities related to the band structure in the interfacial region were found from an analysis of the EER data.

## IMPROVEMENT OF THE ASE APPARATUS AND CONSTRUCTION OF A HOT CELL

The remaining phase of our investigation has been a continuing attempt to improve the quality of the ASE measurements so that more reliable data could be obtained. These refinements have included improvement of the signal to noise ratio of the apparatus, reduction of the time required for data acquisition, improvement in sample control procedures, and development of apparatus and techniques to allow ASE data to be taken at elevated temperatures. A good signal-to-noise ratio is a necessity for obtaining accurate lineshape data. Third derivatives of the dielectric constants as a function of energy are required to obtain ASE lineshapes, so noise must be kept to a minimum. An improved predispersing system as well as the reduction of random noise has allowed lineshape determinations to be practical. Further improvement is being pursued, however. Replacement of the digitally controlled predispersing system with a direct drive predisperser has reduced data acquisition times by nearly a factor of two. This allows more frequent sampling of surfaces and allows less time for surface oxidation of the samples. Sample preparation by surface etching before mounting causes too much opportunity for surface deterioration prior to monitoring. An in situ sample cell capable of allowing surface etching in an inert atmosphere immediately prior to data collection has also been developed and allows more reliable values for the dielectric constants to be developed. Finally, a hot cell has been built and operated at elevated temperatures. Variations in measured values of the dielectric constants as a function of temperature have been obtained. Still required, however, is the combining in one cell of a heating capability with an in situ etching capability. Perfection of such



a cell is required before reliable data can be obtained as a function of temperature.

#### The Heat Cell

A cell was needed to modify the ellipsometer in such a way as to allow the temperature of the sample to be changed in a well controlled atmosphere. A description of the design follows.

Body of Cell: This was made of brass; side and top views of the cell are shown in Figures 4 and 5. There are three windows on the cell to allow for the two angles of incidence that are available on the ellipsometer. One arrangement allows for an angle of incidence of  $67.5^\circ$  and a second arrangement allows for a  $45^\circ$  angle of incidence. The top view shows these two arrangements. The windows are 1" windows mounted on flanges which are attached to the body of the cell through formed steel bellows. This allows the windows to be tilted in such a way that the beam of light is normal to the quartz windows at entrance and at exit. All windows are mounted on Viton and O-Rings to seal the cell from the outside atmosphere.

The Heater: (Figure 6) The temperature of the sample is controlled by mounting it on a copper mount that is heated by a conventional (100 watts) heat cartridge impeded inside it. The temperature is controlled by a heat controller. By mounting the thermocouple on the reflecting surface of the sample we are able to measure the temperature very accurately. Figure 7 shows the special clamps that were machined to mount the sample and the thermocouple. A maximum temperature of  $400^\circ\text{C}$  was obtained by this arrangement. The heat cartridge is mounted on the top of the cell, where we have two parts to allow for circulation of the desired gas.

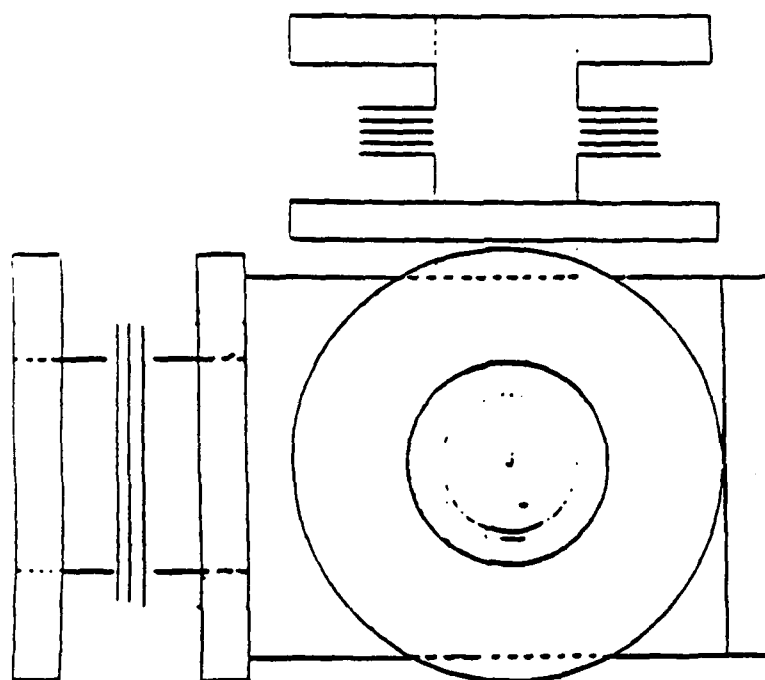
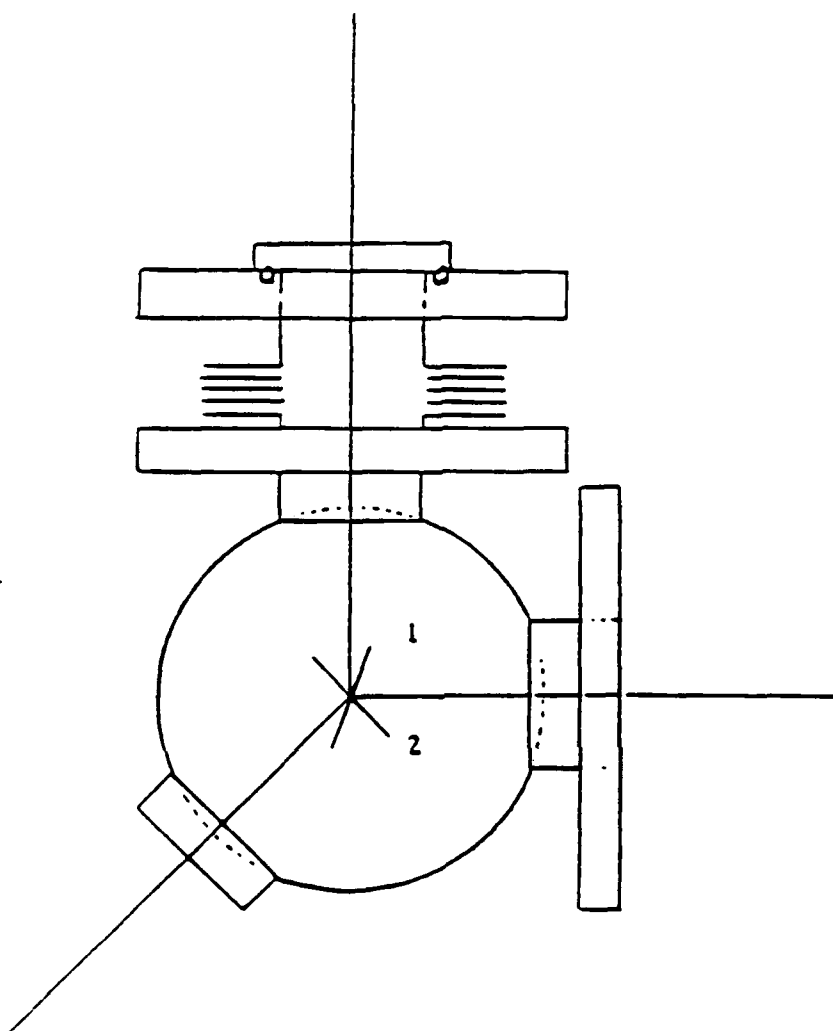


FIGURE 4: Side view of cell showing 2 windows only. Top Flange is used to mount heater and provided with bellows to tilt sample inside cell.



1 is sample in  $67.5^\circ$  incidence

2 is sample in  $45^\circ$  incidence

FIGURE 5: Top view of cell showing 3 windows

- 1,2      Gas inlets
- 3      Alumina rod for heat insulation
- 4      Copper mount
- 5      Sample clamps
- 6      Sample
- 7      Thermocouple
- 8      Heater cartridge
- 9      Thermocouple wires
- 10      Heater wires

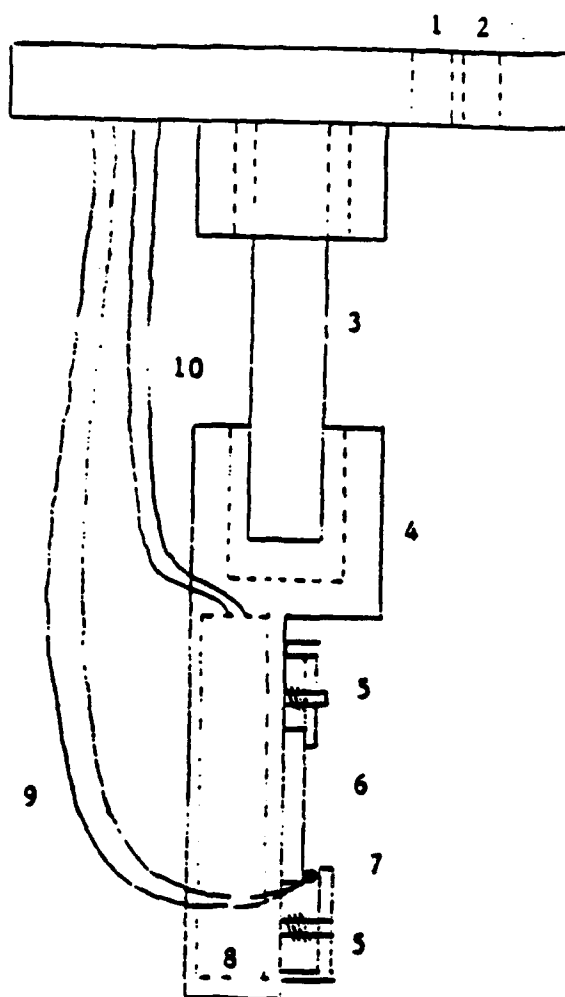
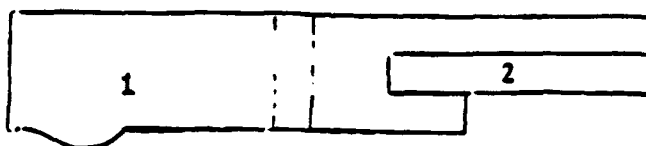


FIGURE 6: Side view of the heater.



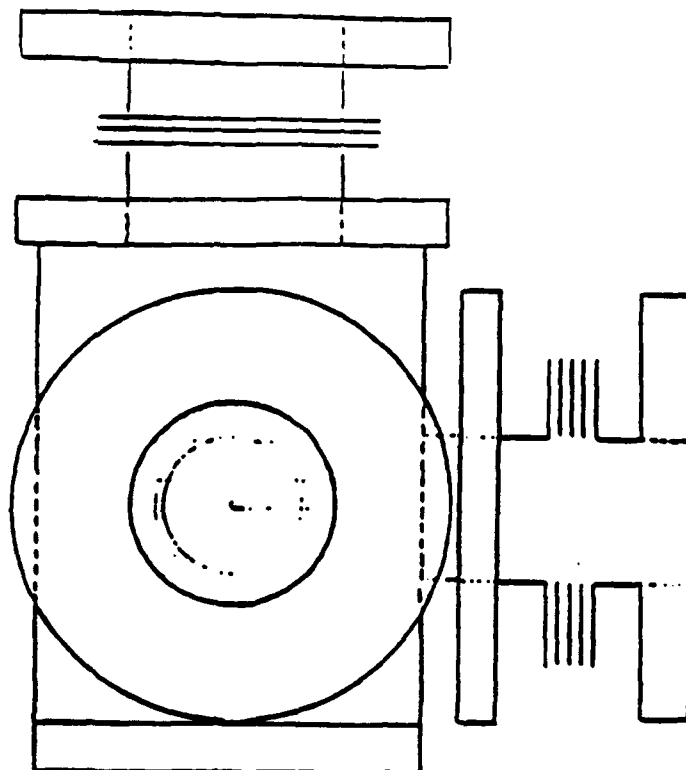
- 1 Sample body made from Aluminum
- 2 Teflon insert to protect sample

FIGURE 7: Special clamps to mount the sample and thermocouple.

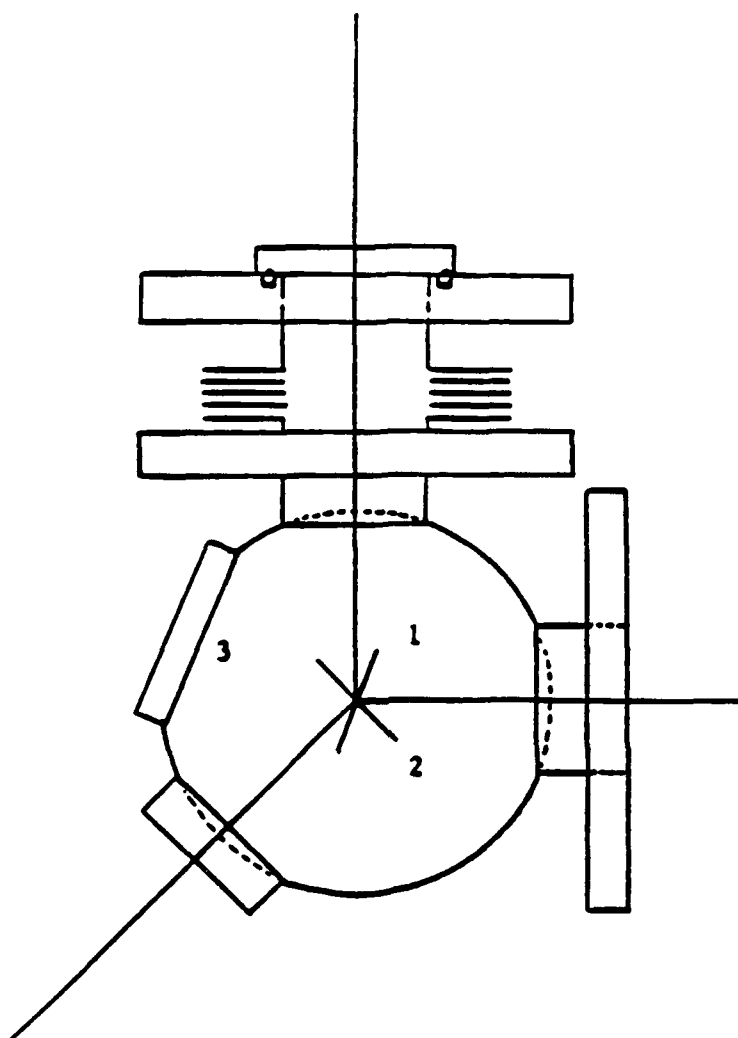
## STATUS OF THE HOT CELL

The "Hot Cell" was needed to study semiconductor surfaces at elevated temperatures in an atmosphere of a mixture of argon and hydrogen gases. The temperatures of interest were believed to range from 20°C to a maximum of 150°C. To meet this need a brass cell was assembled using soft solder. As shown in Figs. 8 and 9, four windows were mounted on the cell. Two reflection configurations of the sample were made possible by utilizing three of the windows in different pairs. One configuration allows for use at an angle of incidence of 67.5° and the other permits use at an angle of incidence of 45°. The 67.5° arrangement which is most frequently used can be very difficult to align. The fourth window mounted opposite the sample mount greatly facilitates this alignment by allowing the direct observation of the beam spot position on the sample. As Figs. 8 and 9 indicate, the windows are mounted on flanges that are attached to the body of the cell through formed steel bellows.

Cell temperature can be elevated by use of a 100 watt cartridge heater embedded in the copper sample mount as shown in Fig. 10. In the presence of Ar-H<sub>2</sub> gas circulation this heater can raise the temperature of the cell to the desired 150°C. However, the cell does act as a heat sink with a huge heat capacity. Heat is conducted to the top of the cell by the circulating gas and the entire cell is heated. This necessitates the use of Kalrez O-rings to withstand the high temperature.



**FIGURE 8:** Side view of cell showing 2 windows only. Top Flange is used to mount heater and is provided with bellows to tilt sample inside cell.



1. Sample position at  $67.5^\circ$  incidence
2. Sample position at  $45^\circ$  incidence
3. Position of observation window

FIGURE 9: Top view of cell showing 4 windows



- 1 = Stainless steel dewar capacity  
- liter of liquid nitrogen
- 2 = Vacuum
- 3 = Sample
- 4 = Heater cartridge
- 5 = Kalrez O-Ring
- 6 = Heater wires
- 7 = To vacuum pump

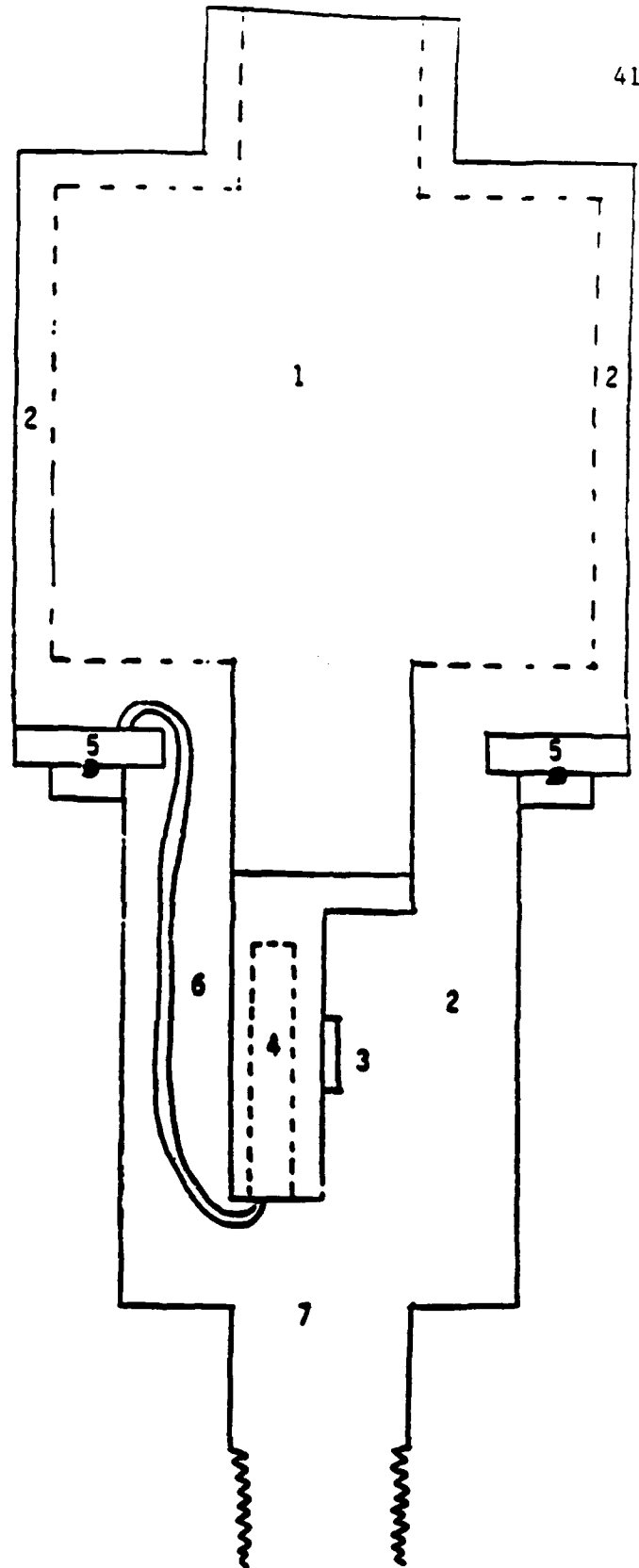


FIGURE 10: Side view of the heater.

### PRELIMINARY ELLIPSOMETRIC STUDIES

Accompanied in Fig. 11 are the results of the real and imaginary parts of the pseudodielectric constants as a function of photon energy obtained from a trial run on a CdTe sample at different temperatures. The sensitivity of these measurements to sample temperature is an encouraging sign for the potential of this ellipsometric technique for studying the temperature dependence of semiconductor surfaces.

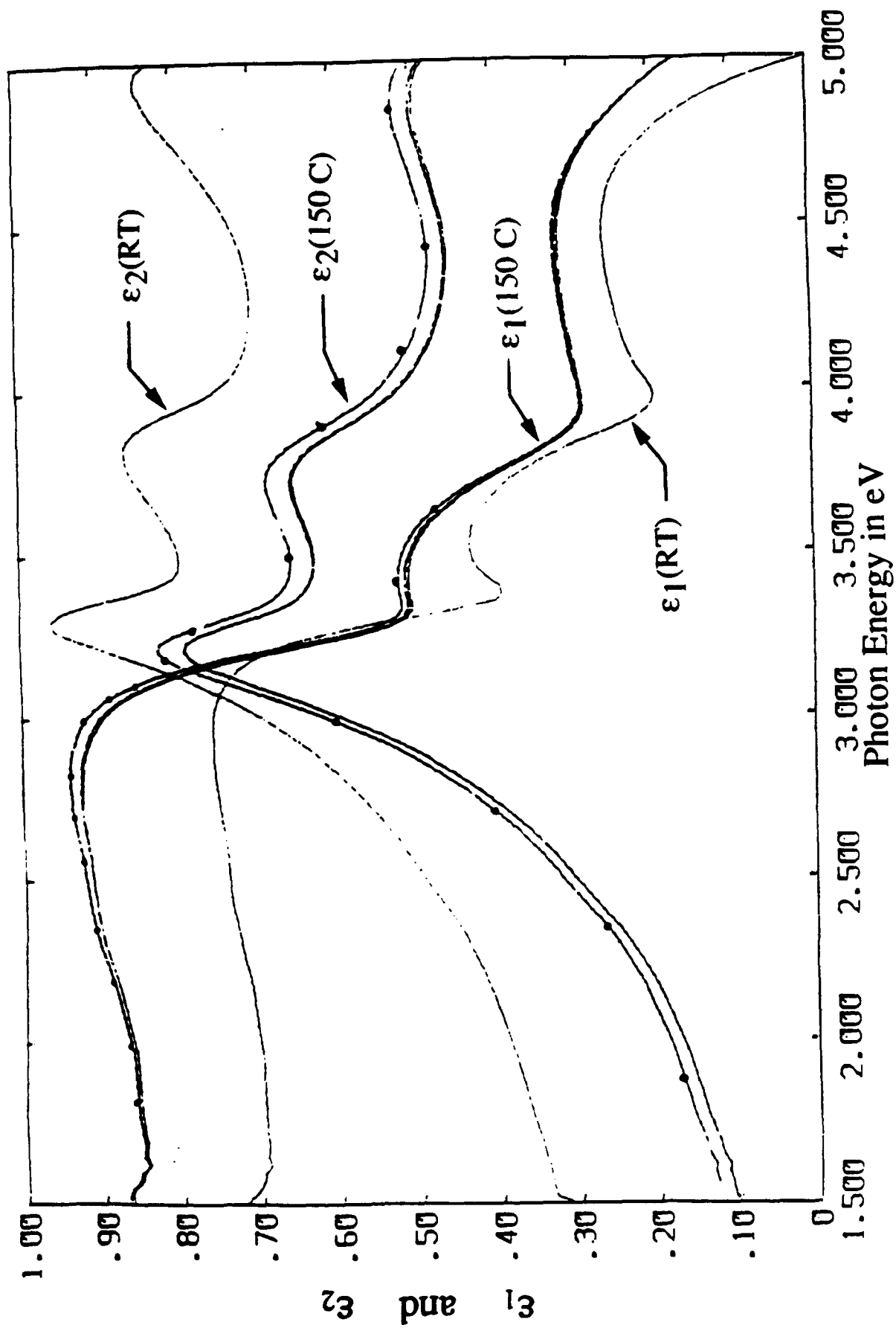


FIGURE 11: Values of  $\epsilon_1(\omega)$  and  $\epsilon_2(\omega)$  for CdTe from ASE measurements at room temperature (RT) and at 150 C. The curves marked with dots include a correction for a surface oxide film.

## PROPOSED IMPROVEMENTS IN THE HOT CELL

On a recent visit Dr. Unchul Lee proposed the desirability of extending the maximum temperature for the temperature studies up to 250°C. This was impossible with the existing cell design. First, the current heater could not heat the sample to that temperature. Moreover, even if a larger cartridge could be accommodated in the cell, the soft solder would melt at approximately 200°C. Changing the solder would amount to building a new cell. Consequently it was decided to heat the samples under vacuum.

Since the visit of Dr. Lee, a new vacuum jacket has been built that will mount on top of the cell. A sketch of the jacket is shown in Fig. 10. In addition to allow heating of the sample, the jacket will allow the sample to be cooled to liquid nitrogen temperatures. A vacuum system has been assembled as well, including a diffusion pump and a cold trap. This system is operational. Since the cell originally was not designed for vacuum, the formed bellows proved very difficult to seal. Moreover, the connection of the cell to the pump had to be made with wet seals that allow the rotation of the cell in measuring the angle of incidence. At present, "cell and vacuum system" together are being tested. It remains to be seen if the vibrations of the pumping system will affect our ellipsometric measurements.

The best vacuum that we can achieve in the cell is of the order of  $10^{-4}$  torr. This will need to be improved. A new cell made of stainless steel pumped by a turbo vacuum pump is under study. Construction of such a cell will yield a much cleaner system than that which a brass cell can provide.

## REFERENCE LIST

1. Unchul Lee, "Characterization of Mercury Cadmium Telluride by Electrolyte Electroreflectance", thesis for Doctor of Philosophy, University of Illinois at Chicago, 1985.
2. P.M. Raccah, U. Lee, J.A. Silberman, W.E. Spicer and J.A. Wilson, "Evidence of Stress-Mediated Hg Migration in  $\text{Hg}_{1-x}\text{Cd}_x\text{Te}$ ", Applied Physics Letters, Vol. 42, No. 4, pp. 374-376, February 1983.
3. P.M. Raccah and U. Lee, "Comparative Studies of Mercury Cadmium Telluride Single Crystal and Epitaxial", Journal of Vacuum Science and Technology, Vol. A 1, No. 3, pp. 1587-1592, July-September 1983.
4. D.E. Aspnes, J.B. Theeten and F. Hottier, "Investigation of Effective-Medium Models of Microscopic Surface Roughness by Spectroscopic Ellipsometry", Physical Review B, Vol. 20, No. 8, pp. 3292-3302, October 1979.
5. P.M. Raccah, J.W. Garland, Z. Zhang, U. Lee, D.Z. Xue, L.L. Abels, S. Ugur, and W. Wilinsky, "Comparative Study of Defects in Semiconductors by Electrolyte Electroreflectance and Spectroscopic Ellipsometry", Physical Review Letters, Vol. 53, No. 20, pp. 1958-1961, November 1984.
6. P.M. Raccah, U. Lee, S. Ugur, D.Z. Xue, L.L. Abels and J.W. Garland, "Study of Mercury Cadmium Telluride (MCT) Surfaces by Automatic Spectroscopic Ellipsometry (ASE) and by Electrolyte Electroreflectance (EER)", Journal of Vacuum Science and Technology, Vol. A 3, No. 1, pp. 138-142, January-February 1985.
7. P.M. Raccah, J.W. Garland, Z. Zhang, U. Lee, S. Ugur, S. Mioc, S.K. Ghandi and I. Bhat, "Study of Mercury Cadmium Telluride Epilayers Grown by Metal-organic Vapor-Phase Epitaxy", Journal of Applied Physics, Vol. 57, No. 6, pp. 2014-2017, March 1985.

8. S.Y. Tong, G. Xu and W.N. Eml, "Vacancy-Buckling Model for the (2x2) GaAs(111) Surface", Physical Review Letters, Vol. 52, No. 19, pp. 1693-1696, December 1983.
9. D.J. Chadi, "Vacancy-Induced 2x2 Reconstruction of the Ga(111) Surface of GaAs", Physical Review Letters, Vol. 52, No. 21, pp. 1911-1914, May 1984.
10. J.P. Faurie, private communication.
11. J.P. Faurie, A. Million and J. Piagnet, "Characterization of  $\text{Cd}_x\text{Hg}_{1-x}\text{Te}$  p-Type Layers Grown by MBE", Journal of Crystal Growth, Vol. 59, Nos. 1/2, pp. 10-14, September 1982.
12. D.E. Aspnes, "Third-Derivative Modulation Spectroscopy with Low-Field Electroreflectance", Surface Science, Vol. 37, pp. 418-442, June 1973.
13. D.S. Kyser and V. Rehn, "Piezoelectric Effects in Electroreflectance", Solid State Communications, Vol. 8, No. 18, pp. 1437-1441, September 1970; V. Rehn and D.S. Kyser, "Transverse Electroreflectance", Physical Review Letters, Vol. 18, No. 20, pp. 848-851, May 1967.
14. R.L. Brown, L. Schoonveld, L.L. Abels, S. Sundaram and P.M. Raccah, "Electroreflectance of Ion-Implanted GaAs", Journal of Applied Physics, Vol. 52, No. 4, pp. 2950-2957, April 1981.
15. B.O. Seraphin and N. Bottka, "Band Structure Analysis from Electroreflectance Studies", Physical Review, Vol. 145, No. 2, pp. 628-636, May 1966.
16. D.E. Aspnes and H. Arwin, "Nondestructive Analysis of Native Oxides and Interfaces on  $\text{Hg}_{1-x}\text{Cd}_x\text{Te}$ ", Journal of Vacuum Science and Technology A, Vol. 2, No. 2, pp. 600-601, April-June 1984.
17. D.E. Aspnes and A.A. Studna, "Schottky-Barrier Electroreflectance: Application to GaAs", Physical Review, Vol. B7, No. 10, pp. 4605-4625, May 1973.

## SUPPORTED WORK (FULLY OR IN PART)

1. P.M. Raccach, J.W. Garland, Z. Zhang, L.L. Abels, S. Ugur and S. Mioc, "Observations of Transitions between Electronic States at the (111) A-Face of CdTe by Electrolyte Electroreflectance", Physical Review Letters, Vol. 55, No. 12, pp. 1323-1326, February 1983.
2. Unchul Lee, "Characterization of Mercury Cadmium Telluride by Electrolyte Electroreflectance", thesis for Doctor of Philosophy, University of Illinois at Chicago, 1985.

## RELATED WORK (PERFORMED UNDER DARPA

CONTRACT #MDA903-82-C-0506)

1. P.M. Raccach, U. Lee, J.A. Silberman, W.E. Spicer and J.A. Wilson, "Evidence of Stress-Mediated Hg Migration in  $\text{Hg}_{1-x}\text{Cd}_x\text{Te}$ ", Applied Physics Letters, Vol. 42, No. 4, pp. 374-376, February 1983.
2. P.M. Raccach and U. Lee, "Comparative Studies of Mercury Cadmium Telluride Single Crystal and Epitaxial", Journal of Vacuum Science and Technology, Vol. A1, No. 3, pp. 1587-1592, July-September 1983.
3. P.M. Raccach, J.W. Garland, Z. Zhang, U. Lee, D.Z. Xue, L.L. Abels, S. Ugur and W. Wilinsky, "Comparative Study of Defects in Semiconductors by Electrolyte Electroreflectance and Spectroscopic Ellipsometry", Physical Review Letters, Vol. 53, No. 20, pp. 1958-1961, November 1984.
4. P.M. Raccach, U. Lee, S. Ugur, D.Z. Xue, L.L. Abels and J.W. Garland, "Study of Mercury Cadmium Telluride (MCT) Surfaces by Automatic Spectroscopic

Ellipsometry (ASE) and by Electrolyte Electroreflectance (EER)", Journal of Vacuum Science and Technology, Vol. A3, No. 1, pp. 138-142, January-February 1985.

5. P.M. Raccach, J.W. Garland, Z. Zhang, U. Lee, S. Ugur, S. Mioc, S.K. Ghandi and I. Bhat, "Study of Mercury Cadmium Telluride Epilayers Grown by Metal-organic Vapor-Phase Epitaxy", Journal of Applied Physics, Vol. 57, No. 6, pp. 2014-2017, March 1985.



## APPENDIX I

SIMPLE APPROXIMATION FOR EFFECT OF ALLOYING  
ON THE PHENOMENOLOGICAL LINEWIDTH  $\Gamma$ 

Consider that  $E_{cv}(\tilde{k})$  is not a unique, sharply defined energy, but that for the absorption of a photon "locally", it depends on the local concentration  $c_{loc}$  averaged over a cluster of  $N$  atoms on the Hg-Cd sublattice.

$$E_{cv}^{loc}(\tilde{k}) = E_{cv}^{loc}(\tilde{k}_{cr}) + \frac{\hbar^2}{2\mu} (\tilde{k} - \tilde{k}_{cr})^2 ;$$

i.e., the dominant source of variation in  $E_{cv}^{loc}(\tilde{k})$  is the variation in the local critical point energy

$$E_0(c_{loc}) = E_{cv}^{loc}(\tilde{k}_{cr}) .$$

Then, for  $N \gg 1$ ,

$$P(E_0) = (\sigma\sqrt{2\pi})^{-1} \exp(-[E_0 - E_0(c)]^2/2\sigma^2)$$

with

$$\sigma^2 = E_1^2 c(1-c)/N ,$$

where  $E(c_{loc}) = E(c) + (c_{loc} - c) E_1$  .

This leads to a replacement of the lineshape

$$L(E, \tilde{k}\Gamma_0) = [E - E_{cv}(\tilde{k}) + i\Gamma_0]^{-1}$$

by

$$L(E, \tilde{k}\Gamma_0) = \int_{-\infty}^{+\infty} (E - E_{cv}(\tilde{k}) - [E_0 - E_0(c)] + i\Gamma_0)^{-1} P(E_0) dE_0$$

A simple analytic result is obtained by expanding  $e^{-u^2}$  as  $[1 + u^2 + \dots]^{-1}$  and keeping only terms to first order in  $u^2$ . This gives

$$\Gamma_m^2 = \Gamma_0^2 + 2\sigma^2 = \Gamma_0^2 + 2E_1^2 c(1-c)/N.$$

For  $\Gamma_0 = 70$  meV and  $c = 0.3$  this gives the following table for  $N$  as a function of  $\Gamma_m$ :

$\Gamma_m$ (meV)	90	110	130	150	170
$N$	181	81	48	33	21

A better numerical approximation leads to values of  $N$  approx. 40% larger than these. For  $\Gamma_0 = 70$  meV and  $N = 8$  our simple approximation gives the following table for  $\Gamma_m$  as a function of  $c$ :

$c$	0.0	0.1	0.2	0.3	0.4	0.5
$\Gamma_m$ (meV)	70	89	102	110	115	116